applied sciences

MDPI

Article

Meteorological Support for the Operation of Unmanned Aerial Systems (UAS) in Hong Kong—Challenges as Demonstrated in Three Sandbox Projects

Ming Chun Lam [1], Yiu Fai Lee [1], Kai Kwong Lai [1], Sze Ning Chong [1], Pak Wai Chan [1,*], Yerin Kweon [2] and E Deng [3]

[1] Hong Kong Observatory, Hong Kong, China; mclam@hko.gov.hk (M.C.L.); yflee@hko.gov.hk (Y.F.L.); lai.kaikwong@gmail.com (K.K.L.); snchong@hko.gov.hk (S.N.C.)
[2] Department of Mathematics (MATH), Hong Kong University of Science and Technology, Hong Kong, China; ykweon@connect.ust.hk
[3] Department of Civil and Environmental Engineering, The Hong Kong Polytechnic University, Hong Kong, China; early.deng@polyu.edu.hk
* Correspondence: pwchan@hko.gov.hk

Abstract

This paper uses test flights of three UAS sandbox projects in Hong Kong as examples to demonstrate the challenges of simulating wind and turbulent kinetic energy (TKE) in meteorological support for unmanned aerial system (UAS) operations. Previous evaluations have focused mainly on mid-latitude continental cities, so the coupling of mesoscale and microscale models remains insufficiently evaluated over the complex terrain and the partially urbanized coastal environment of Hong Kong. To our knowledge, this is the first application of WRF–FastEddy to three real UAS sandbox flights in Hong Kong across different seasons. Two simulation approaches were considered: (1) coupling a mesoscale meteorological model with a computational fluid dynamics model, and (2) using the meteorological model alone with building effect parameterization. The simulated data are compared with the UAS observations and, where available, with vertical wind profiles from Light Detection and Ranging (LiDAR) systems. Two different UAS types were used, covering different seasons in Hong Kong. Across the three cases examined, the simulations systematically underestimated wind speed and the FastEddy prognostic subgrid-scale (SGS) TKE relative to the UAS-derived estimates, irrespective of the assessment platform, the meteorological conditions, or the simulation method. The simulated TKE fields are, however, qualitatively consistent in spatial pattern with the available UAS-derived estimates and help reveal the complexity of the turbulence distribution in the sandbox project areas. This paper highlights the limitations of current technologies and shows that further research, e.g., with different parameterization schemes, is still required.

Keywords: unmanned aerial systems; wind; turbulent kinetic energy; large-eddy simulation; urban meteorology; low-altitude economy

Check for updates

Academic Editor: Nathan J. Moore

Received: 6 October 2026
Revised: 20 November 2026
Accepted: 22 November 2026
Published: 26 November 2026

Copyright: © 2026 by the authors. Licensee MDPI, Basel, Switzerland. This article is an open access article distributed under the terms and conditions of the Creative Commons Attribution (CC BY) license.

1. Introduction

The coupling of a computational fluid dynamics (CFD) model with a mesoscale meteorological model has been applied in many contexts, such as air-quality studies in idealized or real urban street canyons and assessment of the impact of buildings and other man-made structures on localized airflow at an operating airport. For aviation applications, it has proven useful in supporting the low-altitude economy (LAE) by optimizing flight

routes of unmanned aerial systems (UAS). For instance, CFD simulations have been used to predict atmospheric wind in urban environments [1]. The resulting algorithm provides safe and efficient routes, avoiding regions with significant turbulence. In such studies, the computationally demanding CPU-based codes such as PALM [2] have been used for conducting large-eddy simulation (LES), as in [3]. Beyond meteorological support, UAS are increasingly used for applications such as aerial mapping, environmental monitoring and coastal mapping [4], illustrating the breadth of LAE-related activities that ultimately depend on reliable meteorological information.

The LAE has been advancing rapidly in places like Hong Kong. There are various sandbox projects to demonstrate the economic value of UAS applications for logistics, such as delivering food and medicine to relatively remote areas. The Hong Kong Observatory (HKO), as the meteorological authority in Hong Kong, is tasked with providing meteorological support for the LAE, and in this regard the experience gained in high-resolution numerical weather prediction (NWP) modeling at the Hong Kong International Airport (HKIA) for low-level windshear and turbulence projects [5,6] may be applied to these sandbox projects. Following the HKIA experience, mesoscale models such as the Regional Atmospheric Modeling System (RAMS) version 6.3 have been employed in a number of studies of meteorological support for UAS operations in the past, e.g., in [7,8] without explicit consideration of buildings.

A GPU-based CFD model, FastEddy [9], has been made available and several studies have reported on its application to support UAS operations. An earlier application of FastEddy to microscale urban flow is reported in [10]. Moreover, FastEddy has been used in the study of localized airflow, e.g., due to lake breeze [11]. FastEddy offers the option of directly modeling airflow disturbances by the buildings, with the background meteorological field provided by the Weather Research and Forecasting (WRF) model. It is therefore of interest to evaluate WRF–FastEddy for airflow simulation in urban and rural environments under weather conditions outside the United States. Recent studies have also explored the estimation and validation of wind and turbulence from UAS flight telemetry [12,13] and from dedicated sonic-anemometer UAS payloads [14], which provide relevant context for the observational reference used in the present study.

This paper is the first to apply WRF–FastEddy to simulate airflow in three sandbox projects in Hong Kong across different seasons. UAS flights have been conducted for these three locations and the simulations are compared with the UAS observations. The study aims to address the following preliminary questions based on the selected cases:

(a) How well does the mesoscale-CFD model perform in simulating winds in the atmospheric boundary layer, through comparison with UAS-measured/estimated winds and vertical wind profiles from nearby LIDAR systems?
(b) Can the CFD model capture the distribution and absolute value of TKE as measured by the UAS?
(c) What is the impact on the simulation results by explicitly including buildings in the simulation?

The above questions are addressed in this paper using three cases only. Many more cases are required to draw climatological conclusions for Hong Kong. The present study provides preliminary insights into these three questions.

Building on these questions, the objective of this study is to assess, using three real UAS flight cases in Hong Kong, the fidelity with which a mesoscale-CFD (WRF–FastEddy) system and a building-effect-parameterized WRF (Urban Model) can reproduce low-level wind speed, wind direction and turbulent kinetic energy, and to identify the dominant sources of discrepancy for future model development.

2. Model Setup

FastEddy 4.0.1 (URL: https://fasteddy-model.readthedocs.io/en/latest/; source code: https://github.com/NCAR/FastEddy-model, both accessed on 3 October 2026) was used in this study. Three simulations were conducted at different locations: (1) Long Ke Wan, (2) Science Park, and (3) Shenzhen Bay, each with distinct grid configurations and output frequencies. The model domain for the Long Ke Wan simulation was discretized into 88 × 82 × 58 grid cells, with an output frequency of 60 s. The Science Park simulation employed 80 × 290 × 58 grid cells, with an output frequency of 5 s. The Shenzhen Bay simulation used 136 × 138 × 58 grid cells, with an output frequency of 1 s. All simulations adopted a horizontal resolution of 20 m, while vertical grid spacing followed a stretched configuration, with a resolution of 67 m at the reference level and a vertical deformation factor of 0.42. This resulted in vertical grid spacing of about 28 m near the surface and stretching to 142.7 m aloft for grids without terrain.

The WRF model (version 4.4.1) [15] provided the mesoscale boundary and initial conditions for FastEddy. WRF was initialized at 00:00 UTC on each flight day and ran for 12 h, driven by the Global Forecast System (GFS) 0.25° analysis. The WRF configuration comprised three one-way nested domains at horizontal resolutions of 9 km, 3 km and 1 km, with 61 vertical levels (lowest level ~28 m). Physics options included the RRTMG [16] long- and short-wave radiation schemes, the Noah-MP land-surface model [17], the YSU planetary boundary layer [18] scheme, the Thompson microphysics scheme [19], and the Kain–Fritsch cumulus scheme on the outer two domains. WRF outputs were written every five minutes and interpolated bilinearly in space and linearly in time onto the FastEddy grid to provide lateral boundary conditions and the initial field; FastEddy then ran with a 0.05 s timestep to resolve the microscale turbulence.

The WRF model provides the meteorological background driving the CFD FastEddy model. The model domains of WRF and FastEddy are shown in Figure 1a–d, where Figure 1a corresponds to the WRF domain, and Figure 1b–d correspond to the FastEddy simulations at the target locations. For FastEddy, vertical deformation compresses the grid near the surface, where turbulence and fluxes are most intense, and stretches aloft to reduce computational cost. Boundary conditions from WRF-interpolated files were updated every five minutes, ensuring consistent mesoscale forcing on the microscale turbulence resolved by FastEddy. A timestep of 0.05 s (1/20 s) was used in all simulations.

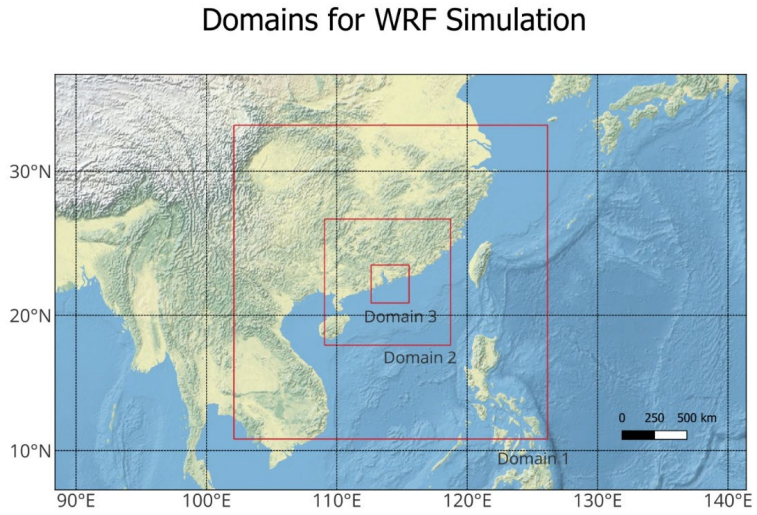

(**a**)

Figure 1. *Cont.*

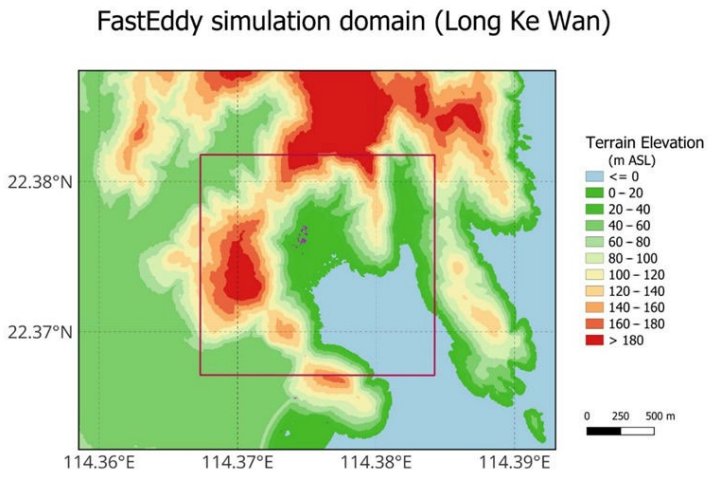

(**b**)

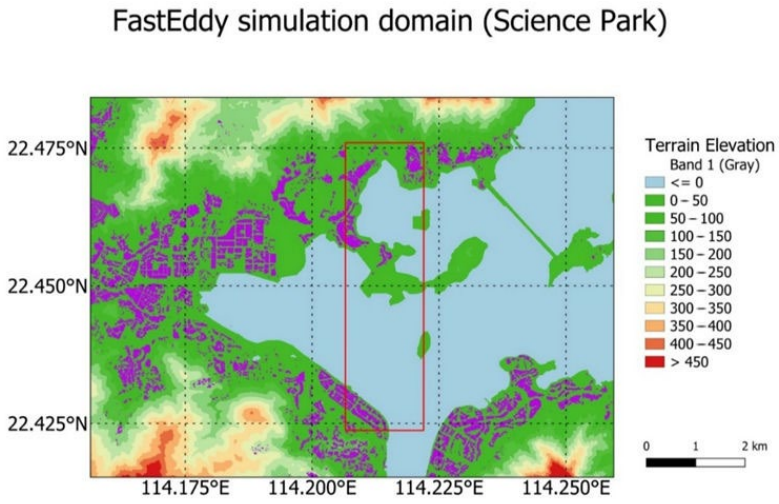

(**c**)

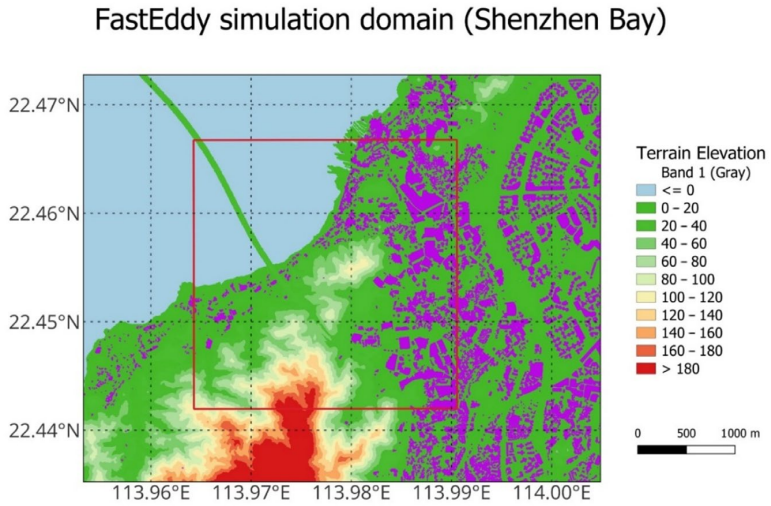

(**d**)

Figure 1. The WRF simulation domains (**a**) and the simulation domains of FastEddy for the three flight routes (**b**–**d**).

Advection used a hybrid fifth-to-sixth order scheme. Moisture was represented by two prognostic species and a condensation scheme, and subgrid-scale diffusion was treated

separately. Turbulence was parameterized using a Lilly/Smagorinsky closure [20–22] with prognostic TKE. The parameterization settings are summarized in Table 1. Surface roughness lengths were derived from the WorldCover 2021 v200 land cover data [23] to construct a roughness map. FastEddy was initialized using boundary and initial conditions derived from WRF simulations, which supplied the mesoscale atmospheric state. These WRF outputs were interpolated onto the FastEddy grid and provide the necessary background fields for temperature, pressure, moisture, and wind.

Table 1. Parameterization settings of FastEddy in the present study.

Parameter	Value	Meaning
Nx,Ny	Long Ke Wan: 88 × 82; Science Park: 80 × 290; Shenzhen Bay: 136 × 138	elements in the x and y directions for the three simulations, respectively
Nz	58	elements in the z direction
d_xi	20	resolution in the “i” direction
d_eta	20	resolution in the “j” direction
d_zeta	67	resolution in the “k” direction
dt	0.05	timestep resolution in seconds
verticalDeformFactor	0.42	deformation factor
verticalDeformQuadCoeff	0	deformation factor
hydroBCs	1	Dirichlet lateral ceiling and surface boundary conditions
ceilingAdvectionBC	1	non-zero w-BC
advectionSelector	3	hybrid 5th–6th order
moistureSelector	1	on
turbulenceSelector	1	Lilly/Smagorinsky scheme
TKESelector	1	Prognostic TKE
canopySelector	0	Off
diffusionSelector	0	Off

Note: d_xi, d_eta and d_zeta are given in meters; dt is given in seconds.

Terrain data were obtained from a 5 m digital terrain model provided by the Hong Kong SAR government, ensuring accurate representation of local topography. Building heights were derived from the “3D Spatial Data 3D-BIT00” dataset, also provided by the Hong Kong SAR government, which contains detailed three-dimensional building models. These datasets were converted into gridded inputs compatible with FastEddy, allowing the simulations to account for terrain elevation and urban structures within the domains.

Turbulent kinetic energy is defined as

$$TKE = \tfrac{1}{2}\left(u'^2 + v'^2 + w'^2\right) \quad (1)$$

where u', v' and w' are the turbulent fluctuations of the three wind components. Following standard boundary-layer practice [24], the fluctuations are obtained over a 60 s window by removing the window mean and the linear trend fitted by ordinary least squares (linear detrending). Detrending removes the systematic change in the mean wind caused by vertical shear during ascent and descent and by horizontal gradients along the flight path, which would otherwise be mistaken for turbulence. However, given the limitation of the instrument, the vertical component w′ is not measured and is assumed to be zero, so that it makes no contribution to TKE. In FastEddy, TKE is a prognostic subgrid variable obtained

from the Lilly/Smagorinsky closure. Because the 1 Hz UAS data resolve turbulent scales that are partly subgrid in the 20 m FastEddy grid, a direct equality between UAS-derived TKE and the model prognostic TKE is not expected; the UAS-derived TKE is therefore used here primarily as a relative (spatial-pattern) benchmark, and absolute-value comparisons are interpreted with this scale mismatch in mind. Throughout this paper, the two quantities are referred to separately: the 'UAS-derived TKE estimate' is the two-component estimate from Equation (1) with $w' = 0$, and the 'FastEddy prognostic SGS TKE' is the subgrid-scale TKE of the Lilly–Smagorinsky closure. They are not equivalent and are not compared as such; the comparison is used only to assess relative spatial and temporal patterns and the sign and approximate magnitude of the discrepancy.

The root-mean-square error (RMSE) and the correlation coefficient (r) are used to compare the simulated and observed wind speeds, and are defined as

$$\mathrm{RMSE} = \sqrt{(\Sigma(y_i - x_i)^2/n)} \tag{2}$$

and

$$r = \Sigma(x_i - \overline{x})(y_i - \overline{y}) / \sqrt{\left(\Sigma(x_i - \overline{x})^2 \Sigma(y_i - \overline{y})^2\right)}, \tag{3}$$

where x_i and y_i are the observed and simulated wind speeds, $\overline{x}$ and $\overline{y}$ are their means, and n is the number of samples. Because r measures agreement in pattern rather than in amplitude, it must be interpreted together with the RMSE. The mean bias and mean absolute error (MAE) are also used: bias $= (1/n)\Sigma(y_i - x_i)$ and MAE $= (1/n)\Sigma|y_i - x_i|$, with the same notation; a negative bias therefore indicates model underestimation.

For comparison with the UAS observations, the FastEddy output was collocated with each UAS record in both space and time. The UAS position (latitude, longitude and geometric altitude) was first converted to the FastEddy terrain-following coordinate, and the four horizontal grid cells surrounding the UAS location were bilinearly interpolated, with linear interpolation in the vertical to the UAS height above ground level (AGL). Temporal matching used linear interpolation between FastEddy output frames (1, 5 or 60 s, depending on the case) to the UAS timestamp (recorded at 1 Hz). No vertical or temporal averaging was applied beyond this collocation; the impact of collocation choices is discussed in the Limitations section.

Two levels of evaluation are used, and their evidential status differs. The UAS comparison is qualitative and pattern-level: the UAS samples a moving, three-dimensional trajectory at 1 Hz, whereas FastEddy provides a 20 m Eulerian grid, so the two sample different volumes and scales, and the UAS-derived winds and TKE carry platform-related uncertainty. The UAS comparison therefore assesses whether the model reproduces the observed wind regime, temporal evolution and spatial pattern of TKE, not pointwise quantitative skill. The LIDAR comparison is quantitative: the LIDAR provides vertical profiles at fixed sites, matched to the WRF grid cell in space and height, and r and RMSE are reported as formal skill measures. The LIDAR comparison evaluates the WRF mesoscale forcing that drives FastEddy, not FastEddy itself. For the same reason, the UAS statistics report bias, MAE and RMSE but not r: a pointwise correlation along a moving trajectory through a spatially varying field conflates spatial and temporal variability and is not a meaningful skill measure for this sampling geometry.

3. Flight No. 1—Long Ke Wan on 21 January 2026

Long Ke Wan is a bay in the eastern part of Hong Kong. The sandbox project involves delivering materials across the bay to a low hill; winds along the valley and in the bay area are therefore important for determining the safety of delivery of materials from the bay. Localized wind flow may be disturbed by the complex terrain, resulting in uneven wind distribution and slightly higher turbulence (expressed as TKE). The orography of the bay is

shown in Figure 2. The trial flight route is also shown; the UAS flew across the bay several times, climbing and descending the hills. The inset of Figure 2 shows the terrain elevation and the flight route, which broadly follows the terrain shape. The UAS was a DJI M350 RTK; technical specifications are given in Table 2. The flight took place in winter (January).



Figure 2. The orography in Long Ke Wan and the flight route (green). The inset shows the vertical cross section of the flight route.

Table 2. Specifications of the UAS in flight numbers 1 and 3.

Category	Specification	Details
UAS Platform	Manufacturer	DJI
	Model	M350 RTK
	Dimensions (unfolded, excl. rotors)	810 mm × 670 mm × 430 mm (L × W × H)
	Weight	6.47 kg
	Maximum Payload	2.73 kg
	Maximum Wind Speed Tolerance	12 m s^{-1}
	Maximum Flight Time	55 min
	GNSS Systems	GPS, GLONASS, Beidou, Galileo
Meteorological Sensors	Temperature & RH Sensor	Vaisala HMP110
	Wind Speed & Direction Sensor	LICOR LI-550 Sonic Anemometer
Data Processing	Data Storage & Processing Unit	Soarability Sniffer4D Mini2
	Data Frequency	1 Hz

The FastEddy simulation was initialized at 03 UTC of the day (local time = UTC + 8 h) and ran until the evening of that day (09 UTC), covering the entire flight period. The model results were compared with the UAS observations, for horizontal wind speed, wind direction and TKE in Figure 3a to Figure 3c, respectively. In general, the simulated wind speed and direction follow the trend of the actual observations, but the simulated speed tends to underestimate the observed values. Moreover, as shown in Figure 3c, the FastEddy

prognostic SGS TKE is generally lower than the UAS-derived TKE estimate. Investigation of the quality of the UAS-derived TKE, which may be affected by the attitude of the UAS itself, is ongoing. However, even for portions of straight and generally level flight of the UAS, the FastEddy prognostic SGS TKE tends to be lower than the UAS-derived TKE estimate.

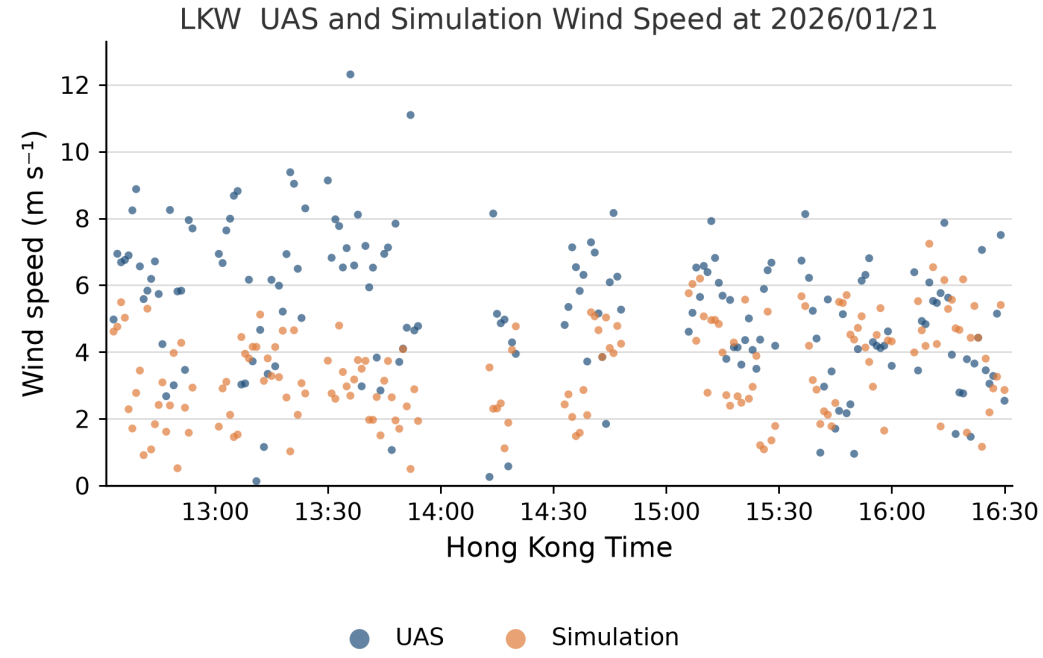

(**a**)

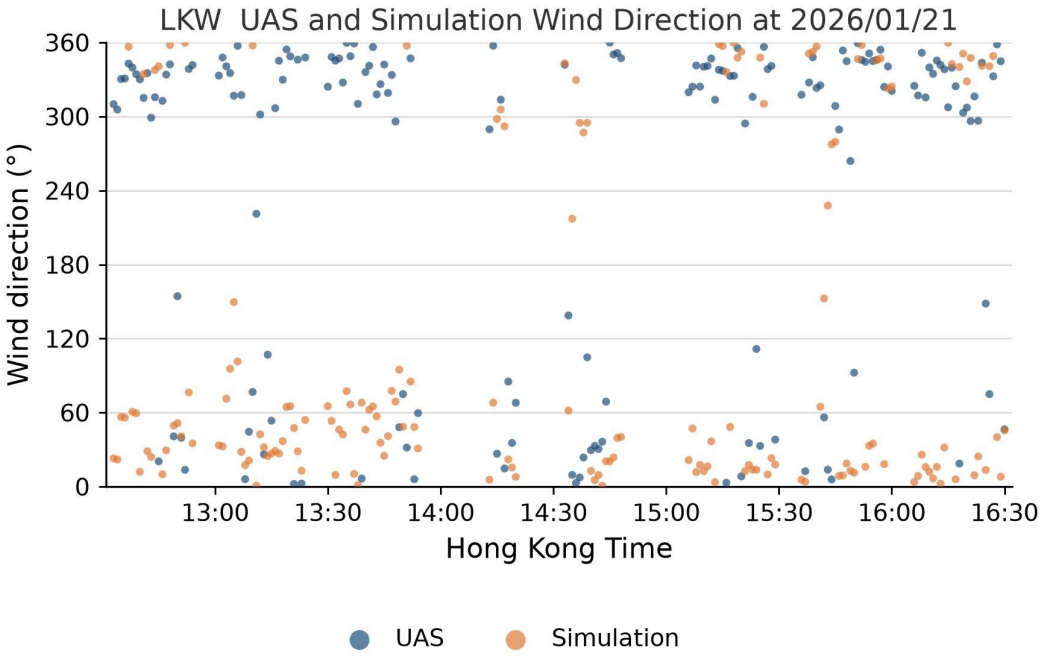

(**b**)

Figure 3. *Cont.*

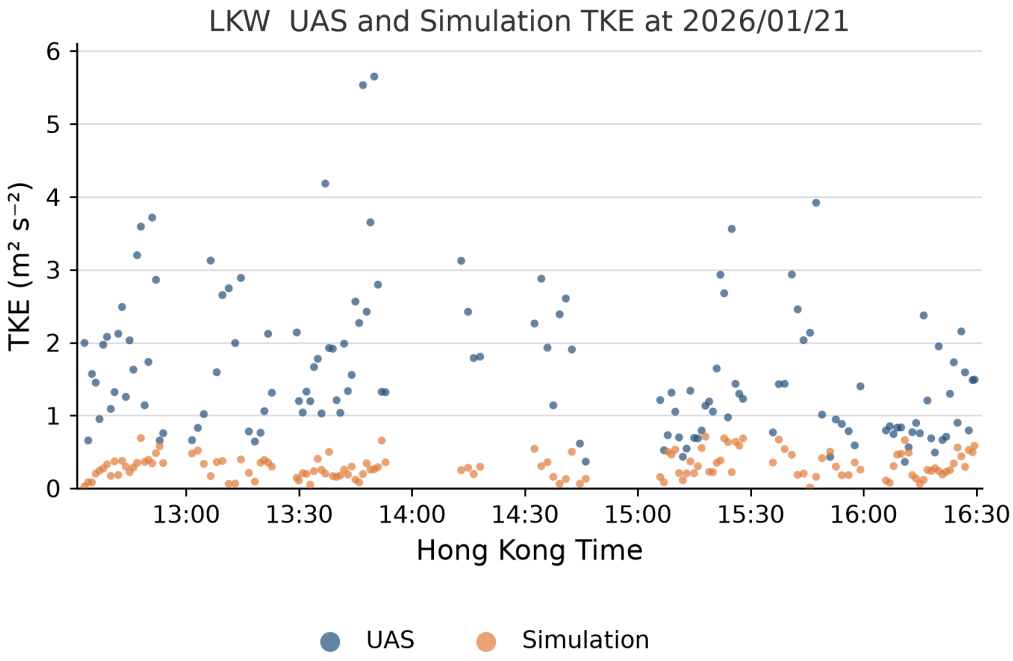

(**c**)

Figure 3. Time series of UAS observations and FastEddy simulation results for flight no. 1: (**a**) wind speed; (**b**) wind direction; and (**c**) TKE.

A spatial distribution plot of the UAS-measured wind and TKE is shown in Figure 4a. The prevailing wind direction on that day was northwesterly, but in the northern part of the flight route, up-valley flow appeared in some sections of the route, possibly associated with daytime heating of the valley and the hilltop (the local time is early afternoon in Figure 4a). Moreover, the measured TKE was higher up the valley as well as on the southern side of the bay.

The model-simulated TKE distribution at a height of 100 m above ground level is shown in Figure 4b. In the simulated TKE field, areas of higher turbulence emerge over the hills in the region, one spreading toward the southern side of the bay (area A in Figure 4b) and another affecting the up-valley route at the northern part of the flight (area B in Figure 4b). The locations of these areas of higher turbulence are qualitatively consistent in spatial pattern with the UAS-derived TKE distribution. As such, though there are differences in the absolute values of TKE (e.g., as shown in Figure 3c), the spatial distribution of the simulated TKE is qualitatively consistent with the UAS-derived estimates. This is a qualitative, pattern-level comparison, not a quantitative spatial validation: the UAS samples are sparse and irregular along the route, and the two TKE quantities are not equivalent (Section 2). The heights of 100 m for the TKE field and 10 m for the wind field were chosen because 100 m is representative of the UAS operating altitude in this case and lies within the region of strongest turbulent production, while 10 m follows the standard near-surface diagnostic height used in mesoscale verification; the choice is consistent across all three cases to facilitate comparison.

The model-simulated 10-m wind above ground level at the same time is shown in Figure 4c. Northwesterly flow over the bay is reproduced. Up-valley flow can be found in areas A and B in Figure 4c, corresponding to the similar areas in Figure 4b. The localized terrain is found to affect the airflow and create areas of higher turbulence. This feature is present in the UAS observations and is qualitatively reproduced in the simulation.



(**a**)

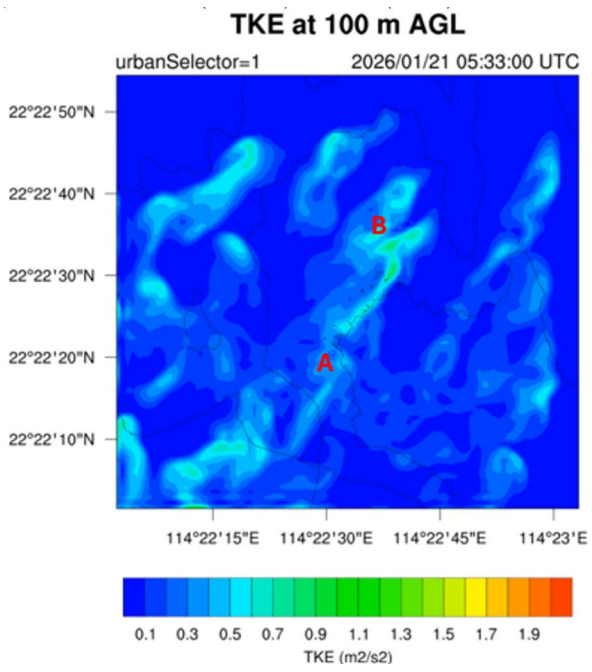

(**b**)

Figure 4. *Cont.*

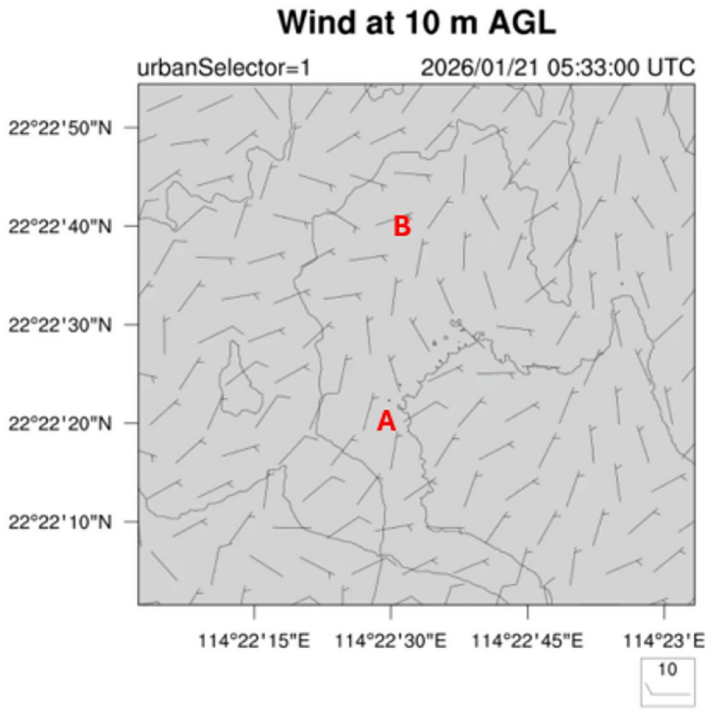

(**c**)

Figure 4. The TKE distribution (colored) and wind (vector) for 13:29 to 13:53 HKT from UAS (**a**), the simulated TKE at 100 m above ground level (**b**) and the simulated wind at 10 m above ground level (**c**).

4. Flight No. 2—Science Park on 22 April 2026

The flight route lies in the northeastern part of Hong Kong; it starts at Science Park, passes an intermediate station on a small island and ends on the other side of the bay, as shown in Figure 5 for the round-trip route between the two locations. The sandbox project delivers food from the more accessible Science Park site to a remote site on the other side of the bay. The UAS was a Keeta Drone FP400-V4; technical specifications are given in Table 3. Fourteen flights were conducted in spring (April) in Hong Kong. The FastEddy simulation ran from 00:00 UTC to 10:00 UTC on 22 April 2026, covering all fourteen flights.



Figure 5. The flight route for Science Park.

Table 3. Technical specifications of the UAS used in flight no. 2.

Category	Specification	Details
UAS Platform	Manufacturer	Keeta Drone
	Model	FP400-V4
	Dimensions (unfolded, excl. rotors)	1360 mm × 1360 mm × 460 mm (L × W × H)
	Weight	7.1 kg
	Maximum Payload	2.4 kg
	Maximum Wind Speed Tolerance	13.8 m s^{-1}
	Maximum Flight Time	27 min (without payload), 16 min (with full payload)
	GNSS Systems	GPS, GLONASS, Beidou, Galileo
Meteorological Sensors	Temperature & RH Sensor	Nil
	Wind Speed & Direction Sensor	A proprietary method for estimating wind speed and direction through the flight control system based on flight data, as opposed to direct measurements from dedicated meteorological sensors.
Data Processing	Data Storage & Processing Unit	Proprietary unit by the manufacturer
	Data Frequency	1 Hz

Note: The Keeta Drone utilizes a proprietary method for estimating wind speed and direction through the flight control system based on flight data, rather than direct measurements from dedicated meteorological sensors; these estimated values have been validated internally by the manufacturer. Similar derived meteorological elements have been extensively discussed in the literature, for example, ref. [12,13]. Whereas flights 1 and 3 employ a sonic anemometer (LICOR LI-550; Table 2) providing direct wind measurements, flight 2 relies on the proprietary estimation described above. The two platforms did not operate simultaneously, so a direct quantitative cross-calibration was not possible within this study. To avoid conflating the two data sources, each case is evaluated independently against its own UAS observations, and the comparison across cases is kept qualitative; a dedicated intercomparison flight with a co-located sonic-anemometer UAS is planned as follow-on work.

The time series of the observed and FastEddy-simulated wind speed, wind direction and TKE are shown in Figure 6a–c. In general, the simulation follows the observed trend for the estimated wind speed and direction, but the former was underestimated. The FastEddy prognostic SGS TKE is generally lower than the UAS-derived TKE estimate.

Sample plots of TKE at 100 m above ground level and wind at 10 m above ground level in the simulation are shown in Figure 7a and Figure 7b, respectively. The wind was generally southwesterly, with higher TKE emerging from the small hill on the southern side of the simulation domain. Higher TKE streaks are also observed over land across the bay. Figure 7b shows reverse flow (light northerly) directly downstream of the hill at the starting point of the route, whereas southwesterly flow generally dominates elsewhere. Limited weather observations were available over the flight route, but available wind data from the automatic weather stations in the region (Figure 7c) are generally consistent with the simulated moderate southwesterly flow.

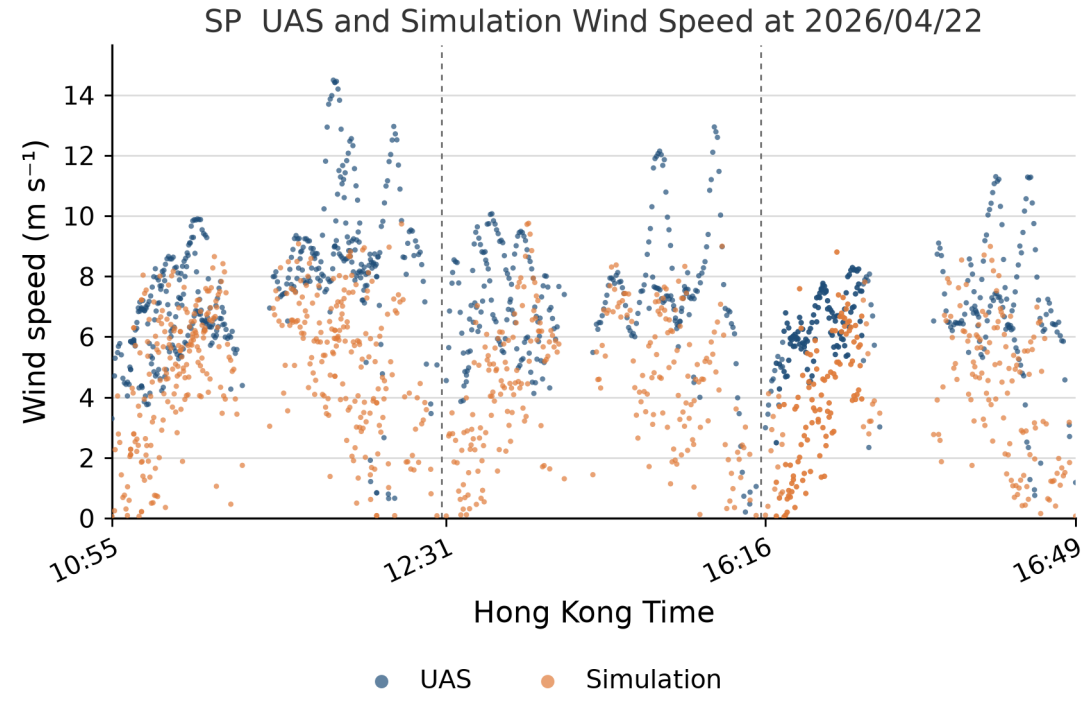

(**a**)

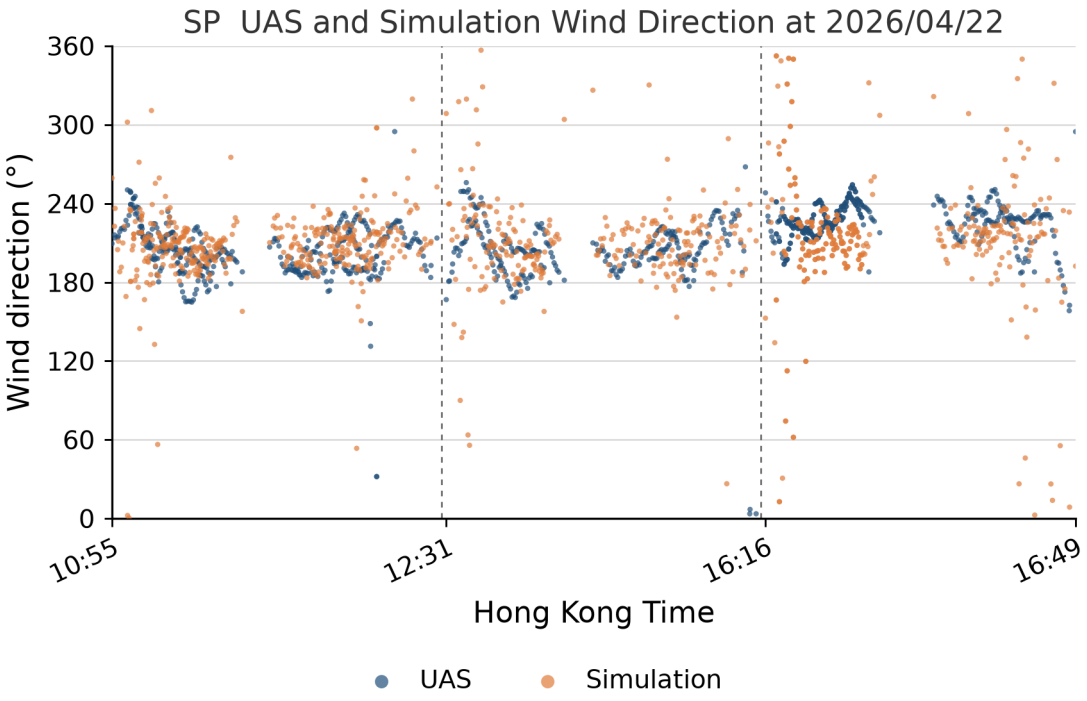

(**b**)

Figure 6. *Cont.*

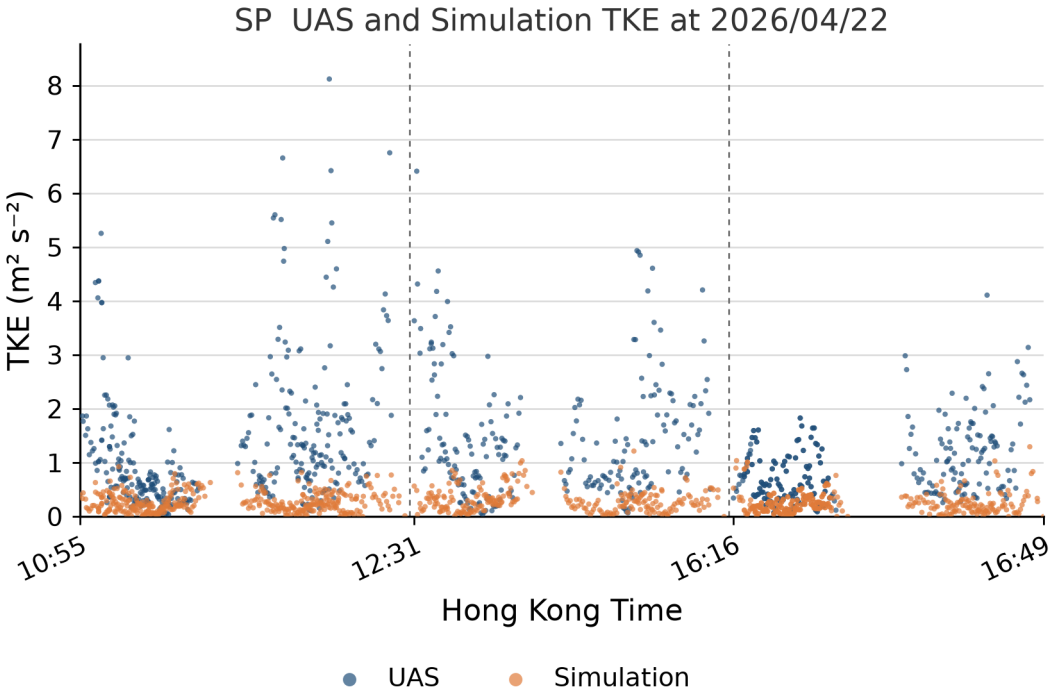

(**c**)

Figure 6. Time series of UAS observations and FastEddy simulation results for flight no. 2: (**a**) wind speed; (**b**) wind direction; and (**c**) TKE. Gaps between flight segments are compressed. Vertical dashed lines mark the segment boundaries.

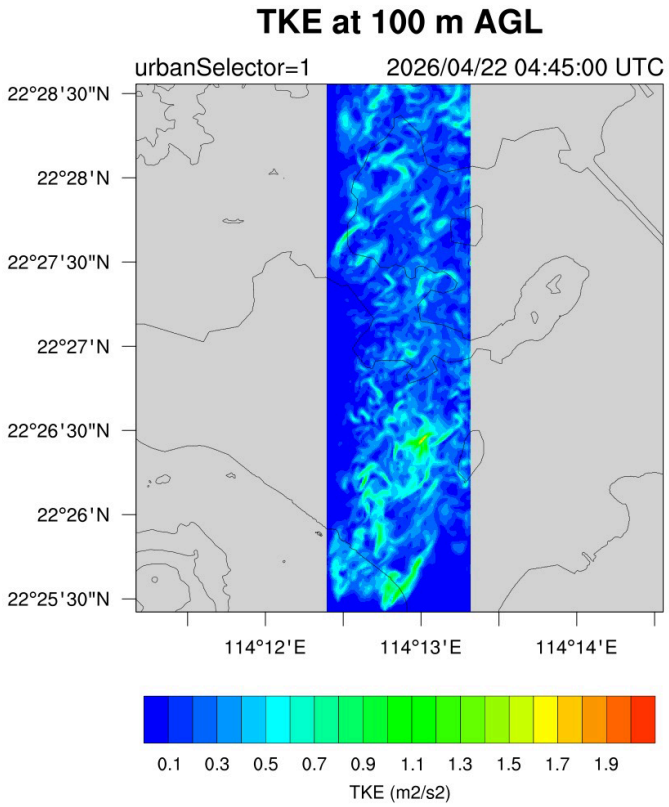

(**a**)

Figure 7. *Cont.*

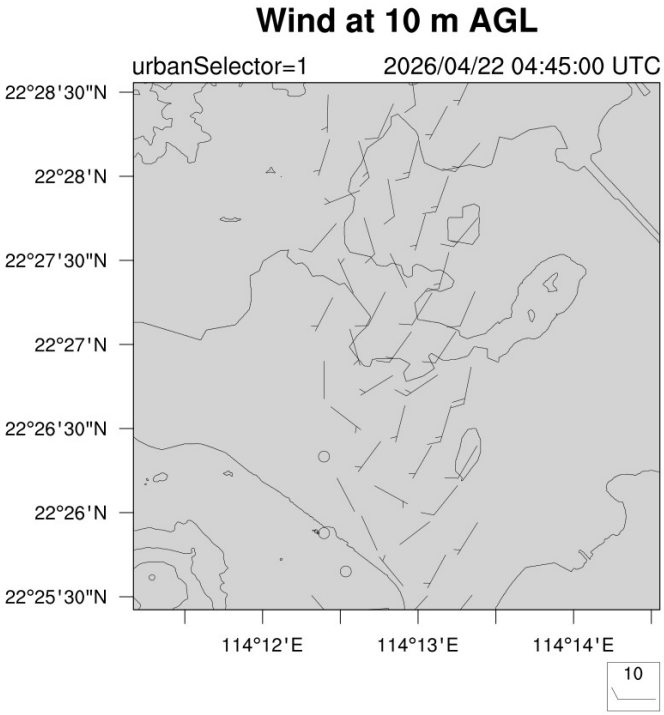

(**b**)

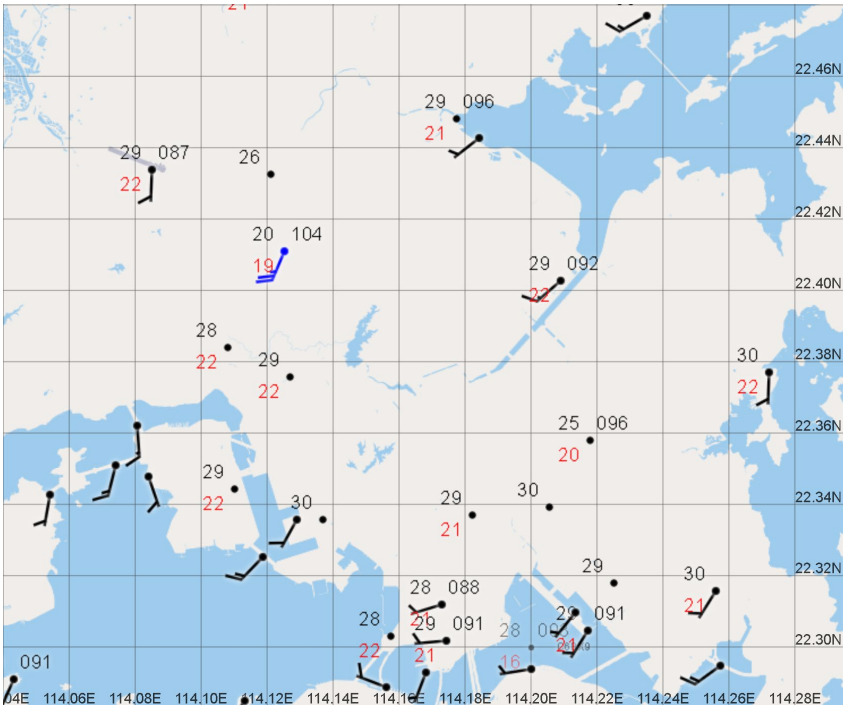

(**c**)

Figure 7. Simulated 100-m TKE (**a**) and 10-m wind (**b**) for flight no. 2; (**c**) weather-station observations around 12:45 HKT on 22 April 2026.

For the current sandbox project, a separate research study has been conducted using a WRF model (without CFD coupling) at a spatial resolution of 200 m in the innermost model domain with building effect parameterization (BEP) [25,26]. This model, also known within the Observatory as the Urban Model, is downscaled from the operational atmosphere-ocean-wave coupled model with a spatial resolution of 1.4 km [27] and has 83 vertical levels (with vertical resolution lower than 50 m below a height of 1000 m above sea level). The

Urban Model primarily aims to resolve the atmospheric boundary layer at higher spatial resolution and to provide a more realistic representation of the urban canopy layer, without explicitly representing buildings, unlike the FastEddy simulation in the previous case. It represents another approach to the issue of meteorological support for UAS operations. Flight no. 2 provides an opportunity to compare the performance of the two approaches. As examples, the flight data from two of the flights are compared with the outputs from the Urban Model and FastEddy simulation: Figure 8a and Figure 8b show wind direction and wind speed comparisons, respectively, in Dataset 7, and Figure 8c,d show the corresponding comparisons in Dataset 11. The two datasets were obtained at different times of the day. The two simulation approaches produce wind directions that are qualitatively consistent with the UAS-estimated wind direction. For wind speeds, the simulation results from the two approaches are comparable, and they generally underestimate the wind speeds estimated from the UAS flight data. For this flight route, both simulation approaches produce comparable results, and in these cases the simulations underestimate the wind speed by a few m s^{-1}.

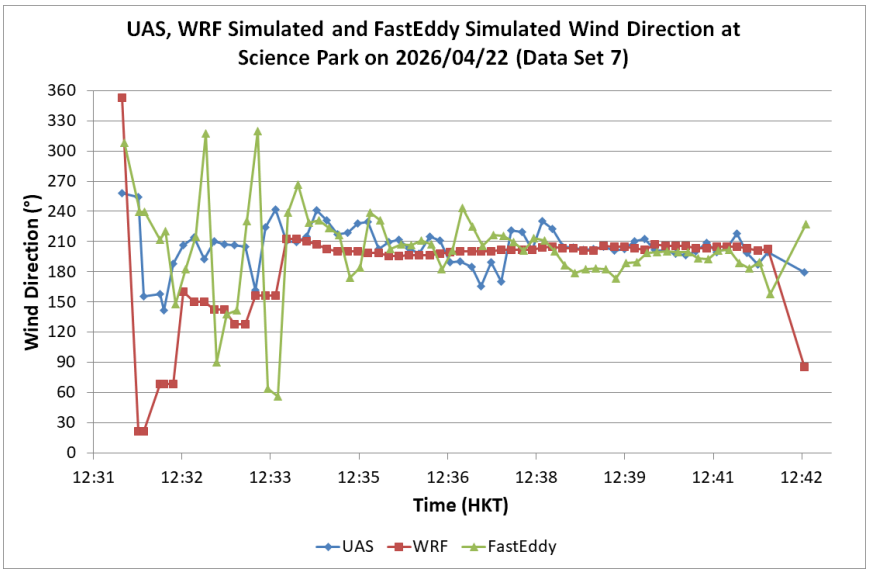

(**a**)

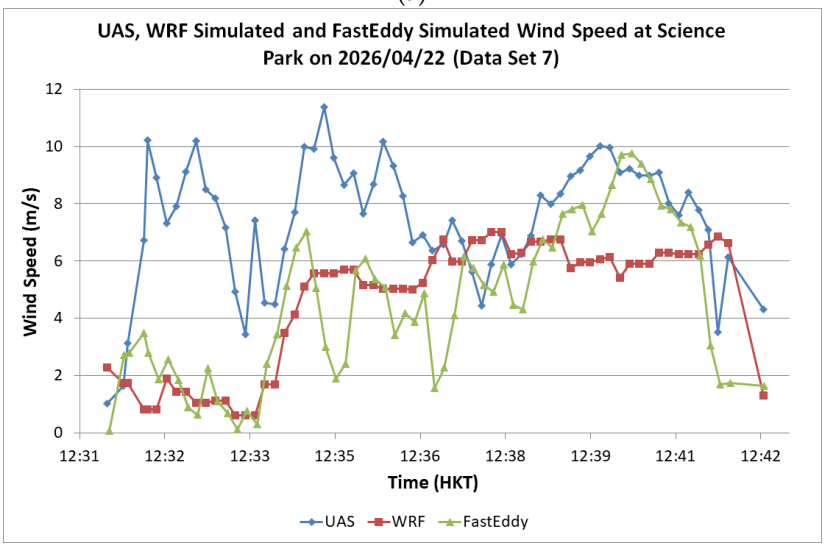

(**b**)

Figure 8. *Cont.*

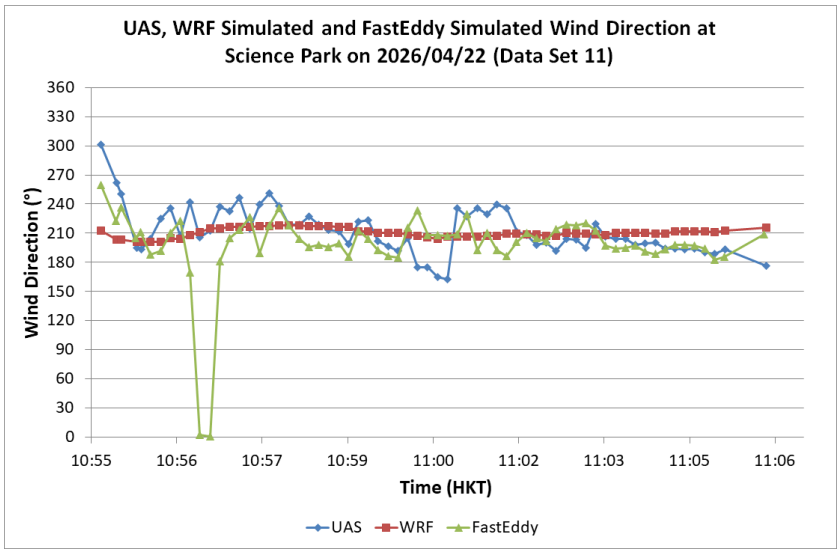

(**c**)

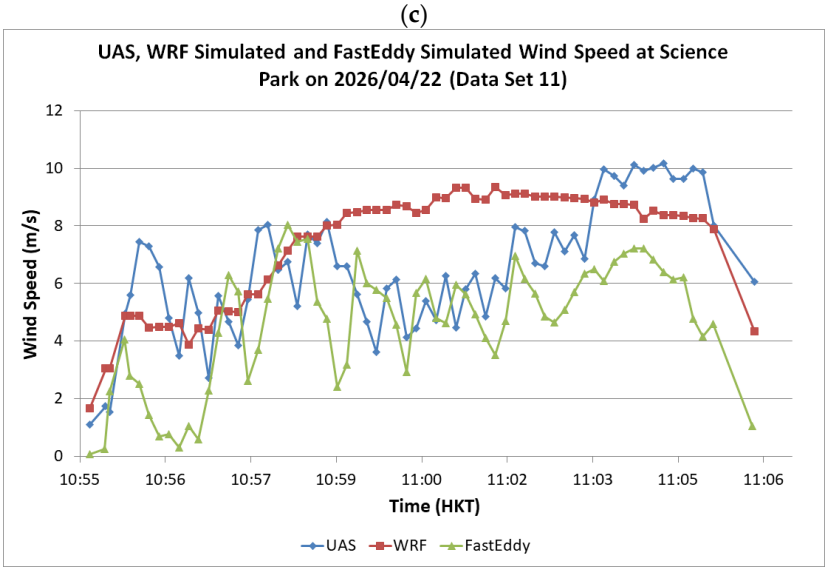

(**d**)

Figure 8. Comparison of UAS observations with the Urban Model and FastEddy simulations for flight no. 2: (**a**,**b**) for Dataset 7; (**c**,**d**) for Dataset 11.

There is also a LIDAR operating near the flight route, at the Shatin site (red dot in Figure 7c), which provides vertical wind profiles for comparison with the WRF output involved in the FastEddy simulation. The LIDAR provides wind data from 56 m to about 1000 m above ground level. Examples of the time series of wind direction and wind speed data at a height of 398 m above ground are shown in Figure 9a,b, together with the WRF simulation results. The observed and simulated data are generally consistent. The wind speeds at all available heights are compared in the scatter plot of Figure 9c. The correlation coefficient is high (around 0.89) and the root-mean-square error is about 1.5 m s^{-1}. The simulated wind speeds are satisfactory in comparison with the available LIDAR data in the present case. The markedly weaker WRF–LIDAR agreement at Shenzhen Bay ($r = 0.13$) compared with Science Park ($r \approx 0.89$) may plausibly be related to the inland, partially urbanized setting of the Shenzhen Bay LIDAR, where thermally driven local circulations and building-induced channeling are more pronounced than over the open, coastal site at Science Park; a lower PBL top and the proximity of the LIDAR to the complex land–sea contrast may also weaken the mesoscale forcing that WRF supplies to FastEddy. These are plausible contributing factors rather than demonstrated mechanisms: with a single

LIDAR site per case, their contributions cannot be separated, and additional cases would be required.

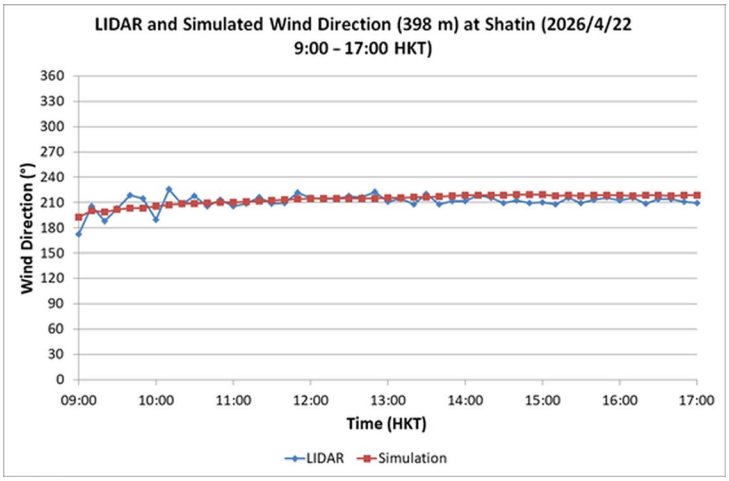

(**a**)

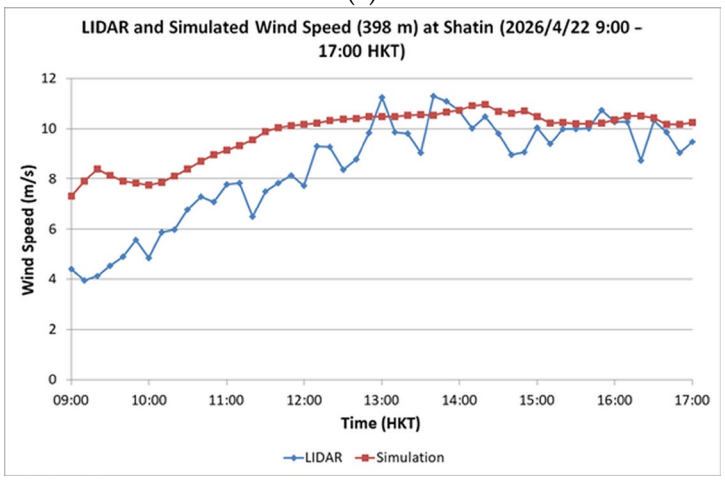

(**b**)

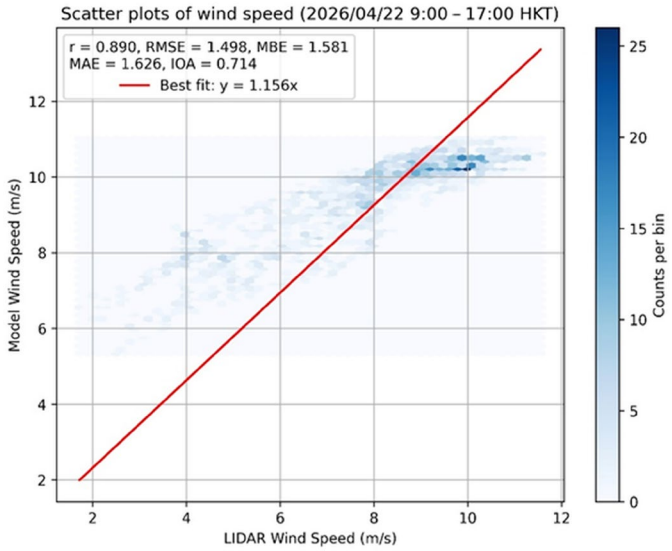

(**c**)

Figure 9. Comparison between WRF simulation and LIDAR data at a height of 398 m above ground level (**a**,**b**); (**c**) scatter plot of the wind speed from the LIDAR observations and the simulations at all available heights.

5. Flight No. 3—Shenzhen Bay on 17 August 2026

The Shenzhen Bay flight is a cross-boundary operation between Shenzhen and Hong Kong, and HKO is responsible for providing the meteorological support for the part of the flight route within the territory. The UAS flies northwest toward the Shenzhen–Hong Kong boundary. The orography and the flight route are shown in Figure 10a and overlaid on a map in Figure 10b as a black curve. In this exercise, a LIDAR is available in the northern part of Hong Kong (location marked by a red dot in Figure 10b) to provide vertical wind profiles for comparison with the WRF simulation results. The UAS was again a DJI M350 RTK (Table 2). The flight took place in summer (August).

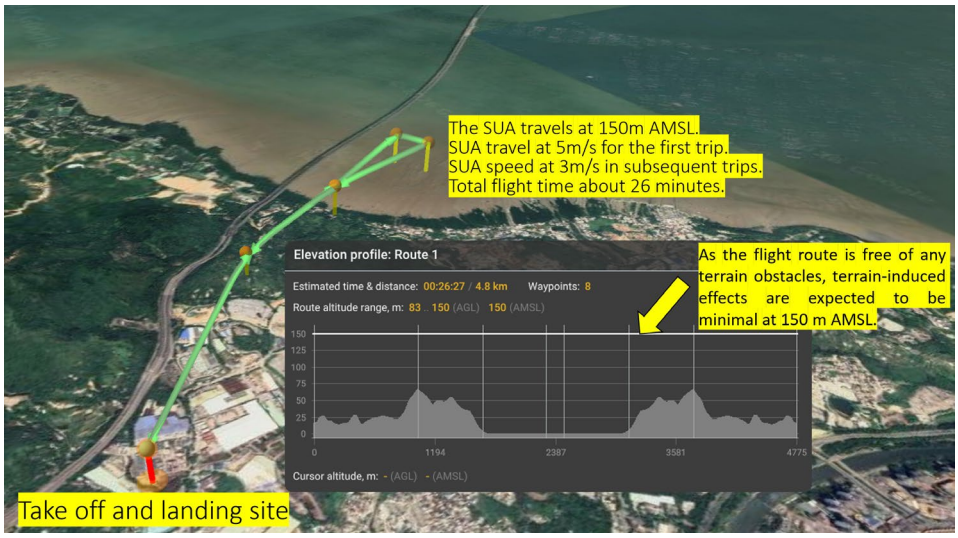

(**a**)



(**b**)

Figure 10. (**a**) Flight route in Shenzhen Bay (green); the inset shows the vertical profile of the route. (**b**) Map of the area.

The FastEddy simulation was initialized at 01 UTC of the day and covered the several flights conducted on that day (up to 09 UTC). The simulation results are compared with the UAS measurements in Figure 11, for horizontal wind speed, wind direction and TKE.

FastEddy tends to underestimate the wind speed. Moreover, as shown in Figure 11c, the FastEddy prognostic SGS TKE is generally lower than the UAS-derived TKE estimate.

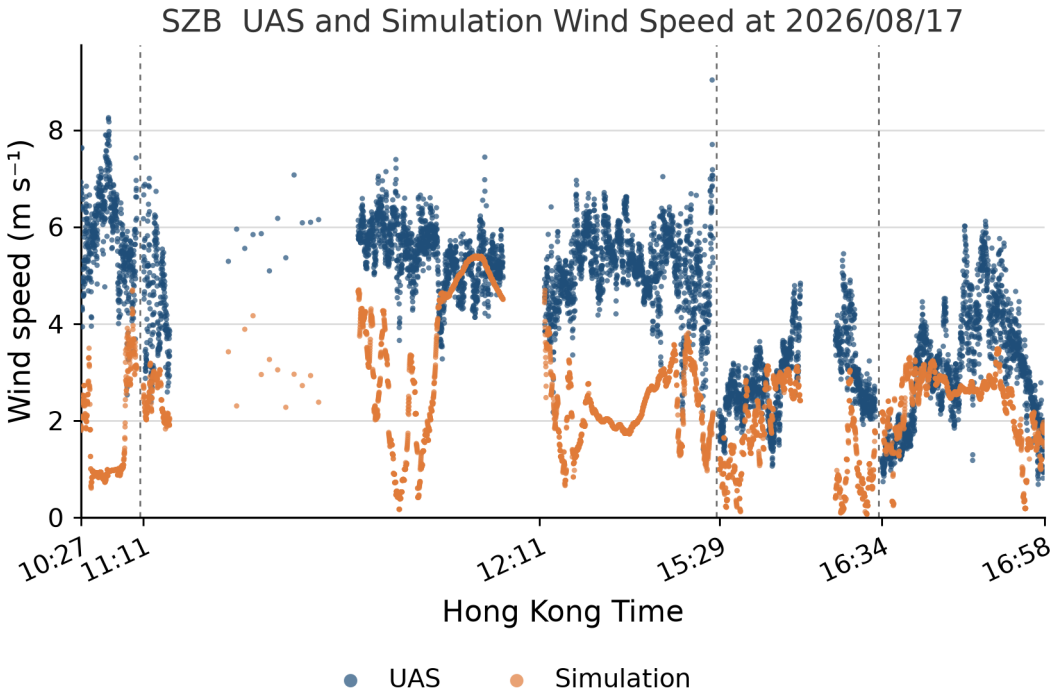

(**a**)

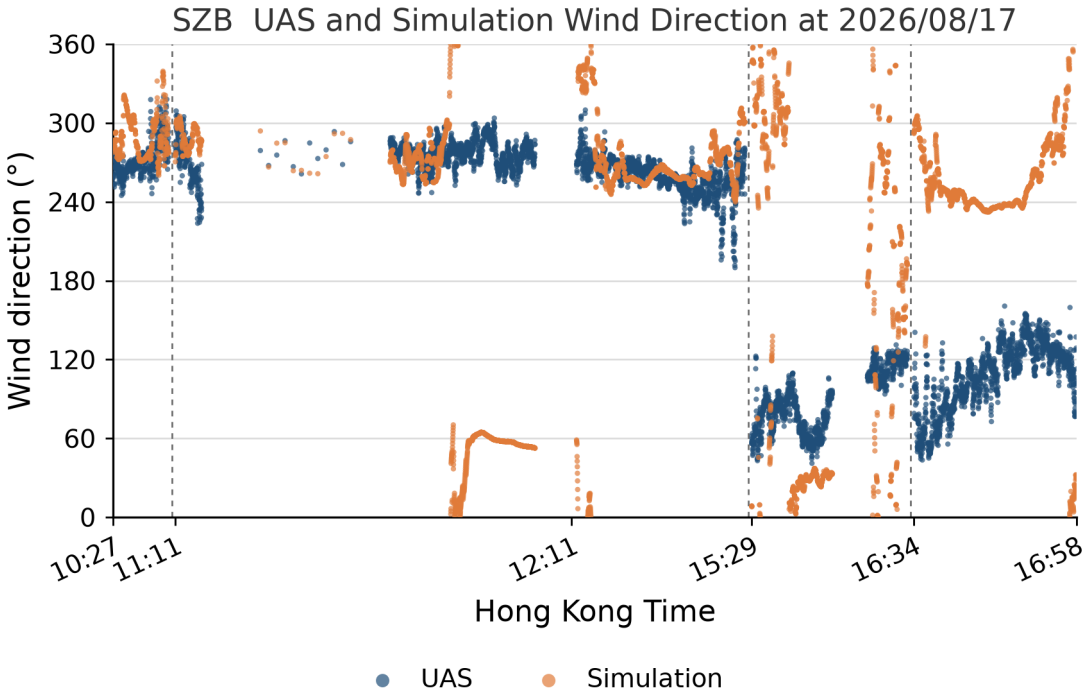

(**b**)

Figure 11. *Cont.*

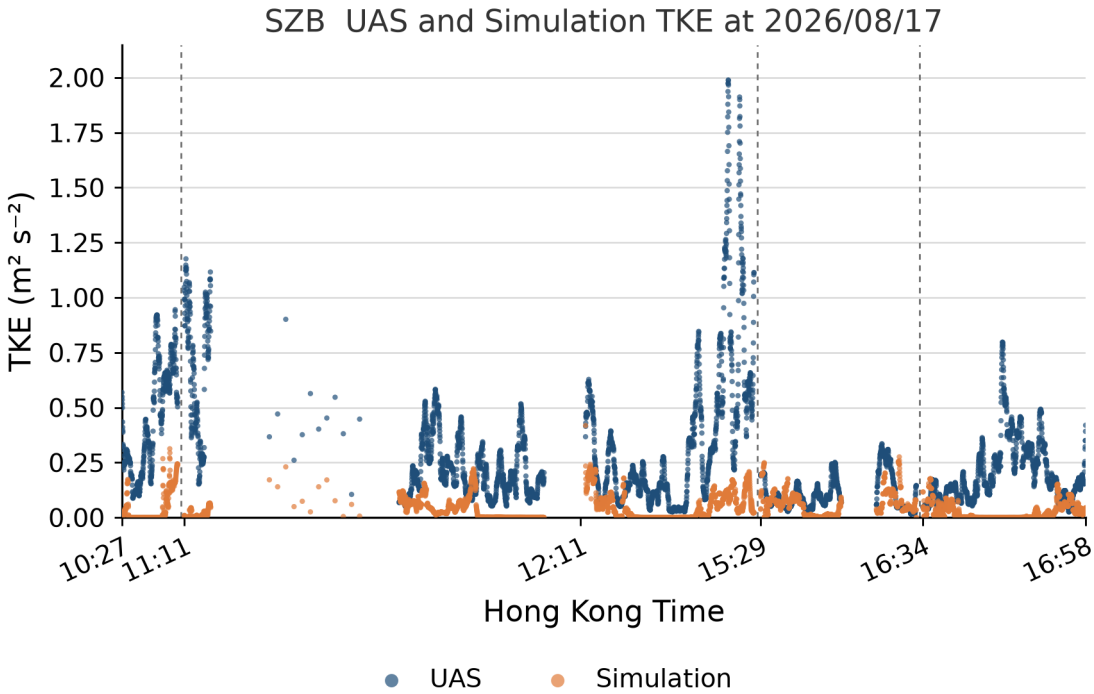

(**c**)

Figure 11. Time series of UAS observations and FastEddy simulation results for flight no. 3: (**a**) wind speed; (**b**) wind direction; and (**c**) TKE. Gaps between flight segments are compressed. Vertical dashed lines mark the segment boundaries.

A spatial distribution plot of TKE and wind as measured on the UAS is shown in Figure 12a, together with the surface weather observations in that region around that time (Figure 12b, with the area under consideration enclosed in red). West to southwesterly winds prevailed on that day. TKE was lower nearer the bay, but increased to higher values inland based on the UAS measurements. The model-simulated TKE at a height of 100 m above ground level is shown in Figure 13a. The simulated and observed TKE fields show three features: (i) there are west–east oriented rows of higher turbulence, which seem to be convective rolls in the atmospheric boundary layer in the westerly flow. The higher turbulence from one such roll was picked up by the UAS measurements in Figure 12a. As such, the simulated and UAS-derived patterns are qualitatively consistent, though the FastEddy prognostic SGS TKE is lower than the UAS-derived TKE estimate; (ii) the simulated TKE is lower over the bay and the adjacent area, qualitatively consistent with the UAS-derived estimates; (iii) there is an area of enhanced turbulence with northeast-southwest orientation at the lower right corner of the simulation domain. Considering the model-simulated 10 m wind (Figure 13b), the higher turbulence may be associated with the convergence between westerly flow to the west and the easterly flow to the east. However, there are no observational data, from either the UAS or the surface weather stations (Figure 12b), to support the appearance of light easterly flow and thus the higher turbulence region. The feature in (iii) above shows that, though Hong Kong is a small place, there are various localized wind features that are still unknown and not readily picked up by the available, already rather densely spaced meteorological instruments.

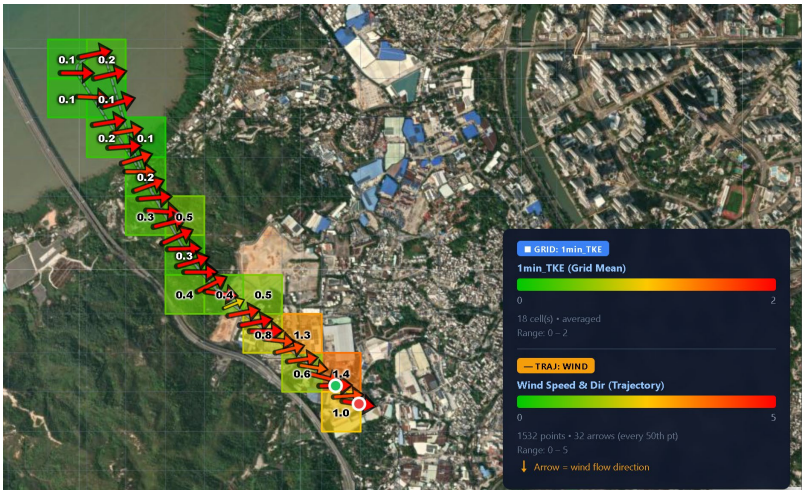

(**a**) TKE (color shaded) and wind (arrow with color shading) at 12:12–12:37 HKT

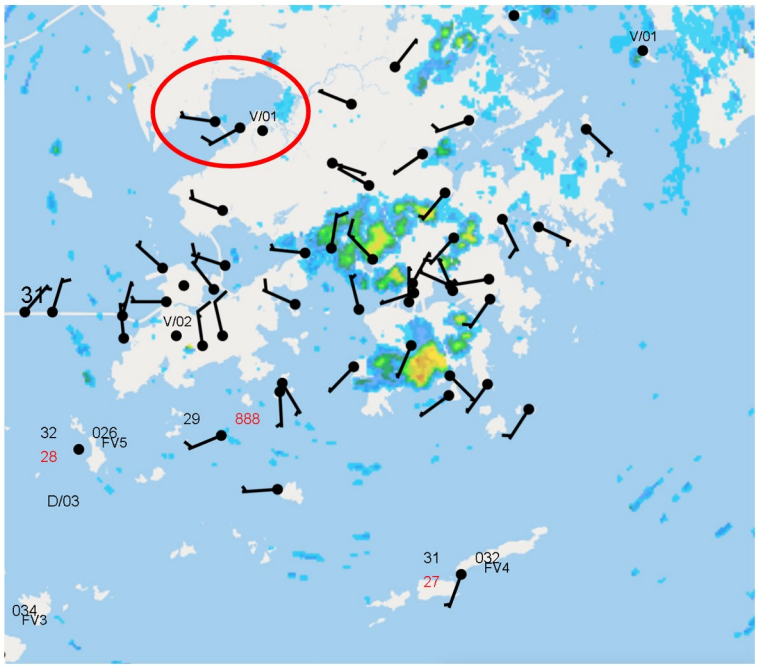

(**b**) weather station observations at 12:15 HKT

Figure 12. (**a**) UAS observations of TKE in colored box and wind vectors; (**b**) nearest weather-station observations for flight no. 3 circled in red.

As shown in Figure 12a, there is an extensive area with low buildings to the east of the bay in Hong Kong. As such, another simulation has been performed without including any buildings in FastEddy, to examine the impact of the buildings on the simulation. The surface roughness configuration was kept the same in the two simulations. The results are shown in Figure 14 for comparison with the UAS measurements. Notably, without the inclusion of buildings, the agreement with the UAS wind speeds was better than in the simulation that included buildings. One hypothesis is that the resolved-building representation imposes an effective drag, and/or increases the effective roughness, that is too large for the low-lying structures in this area, so that the wind speed is further under-predicted. This remains a hypothesis rather than a demonstrated cause: the experiment does not separate building height, building drag, land-cover roughness and grid representation, and further work is needed before a causal mechanism can be established. Based on the result of this experiment, further adjustments are being made to the treatment of building effects on airflow in the FastEddy simulation. Previous simulations at HKIA showed that including buildings reveals

many features of building-induced low-level wind effects on aircraft that cannot be captured otherwise. As such, including buildings remains important for a more realistic simulation of wind speed. One challenge of the present study is that the buildings in the Shenzhen Bay area within Hong Kong territory are much lower than those at the airport (several tens of meters in Shenzhen Bay vs. a few hundred meters at the airport). Some tuning of FastEddy will be required to handle such low-lying buildings and their impact on the very localized airflow. A focused sensitivity study on roughness length and building-height thresholds is planned and will be reported separately.

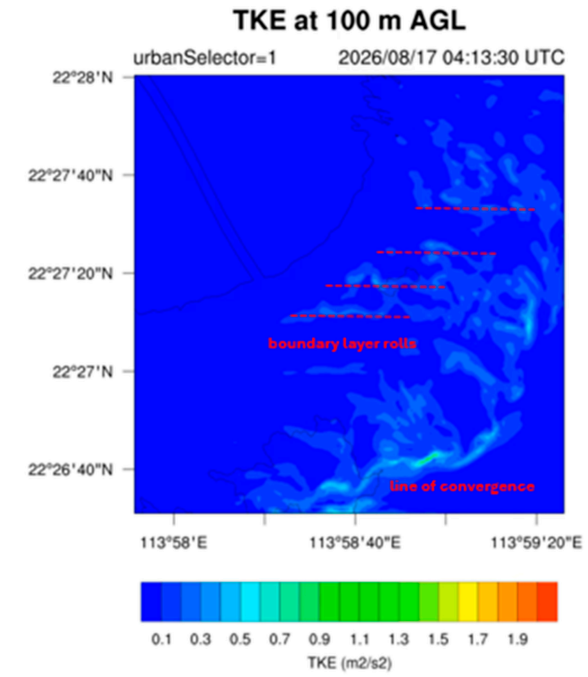

(**a**)

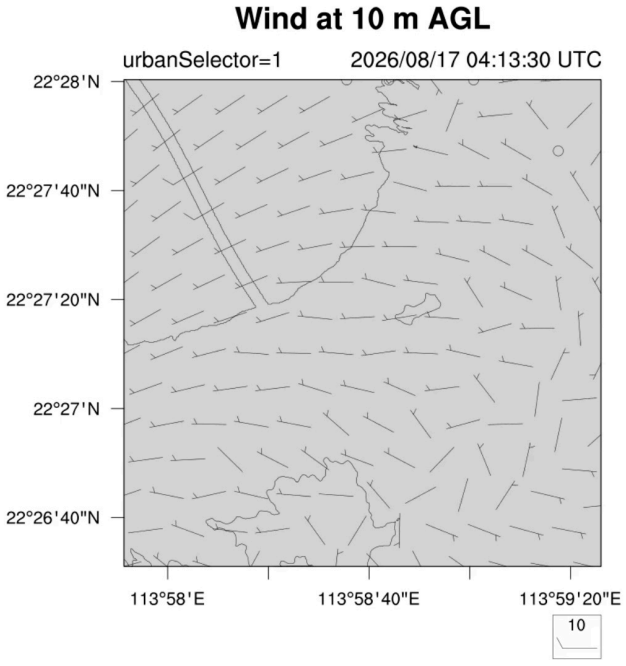

(**b**)

Figure 13. Simulated 100-m TKE (**a**) and 10-m wind (**b**) for flight no. 3.

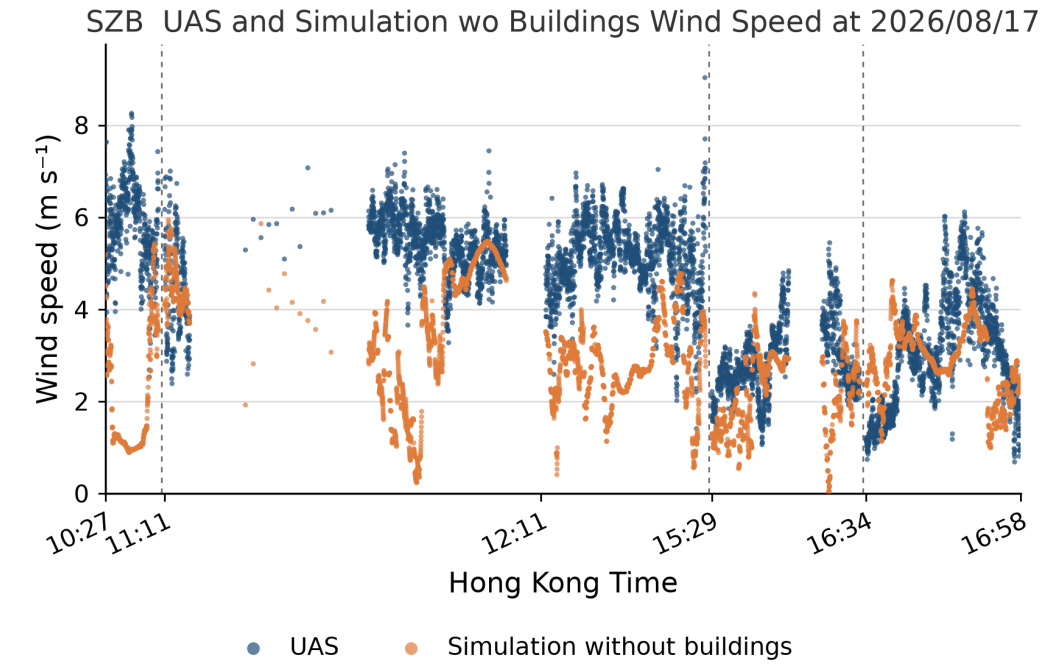

(**a**)

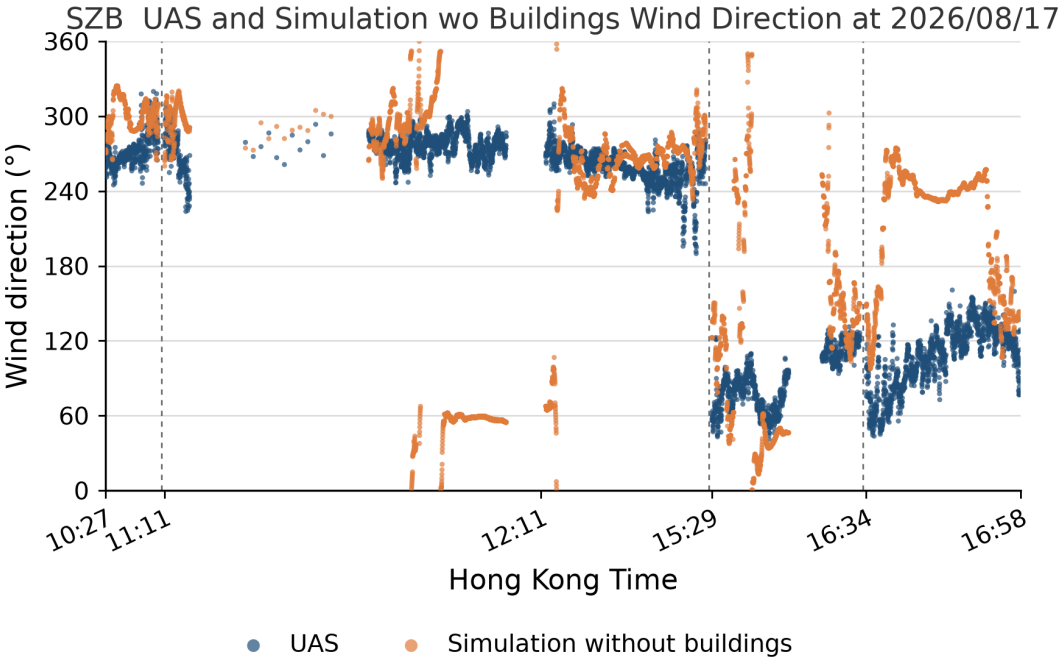

(**b**)

Figure 14. *Cont.*

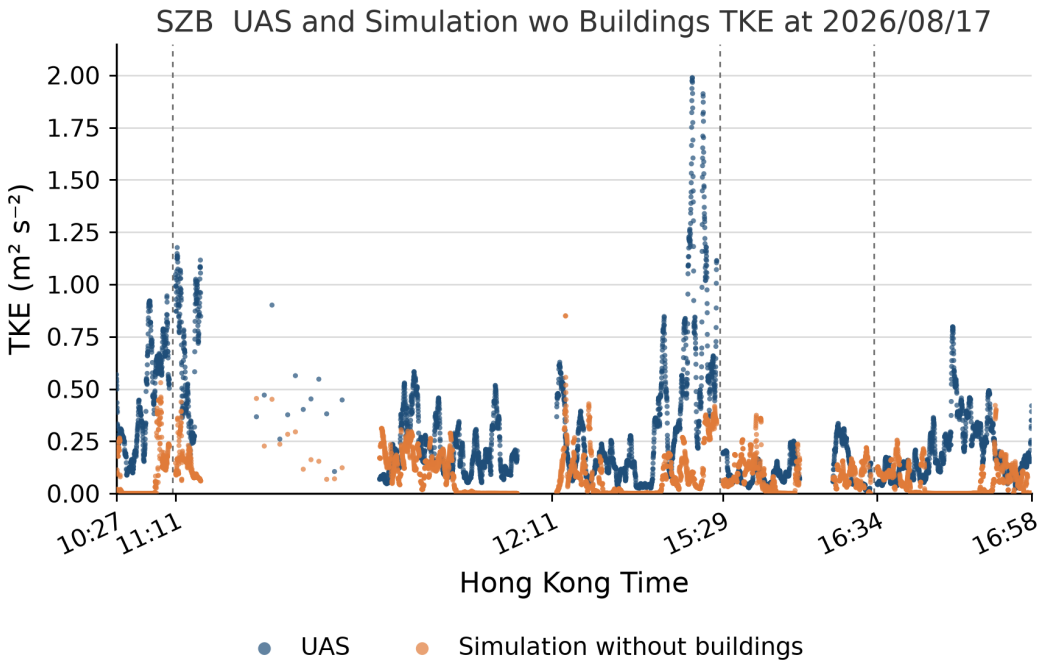

(**c**)

Figure 14. Time series of UAS observations and FastEddy simulation without buildings for flight no. 3: (**a**) wind speed; (**b**) wind direction; and (**c**) TKE. Gaps between flight segments are compressed. Vertical dashed lines mark the segment boundaries.

WRF simulation results are compared with the LIDAR measurements at various heights in Figure 15. The LIDAR measures the wind from 56 m to about 1000 m above ground level, and all available heights are included in the scatter plot of Figure 15c. The time series of the measurements and the simulation results at the selected height of 56 m are shown in Figure 15a for wind direction and Figure 15b for wind speed. From the time series, the WRF simulation captures the general trend of the measured wind direction and wind speed. However, in the scatter plot, WRF is found to underestimate the wind speed, and the correlation with the LIDAR observations is weak ($r = 0.13$). The under-estimation of wind speed by FastEddy may therefore be partly inherited from WRF, especially for the inland area of Hong Kong; with a single LIDAR site, this attribution remains tentative. This is another area that requires further investigation and improvement.

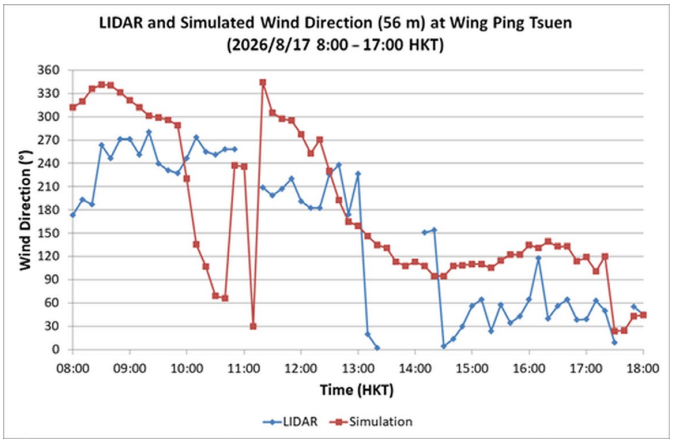

(**a**)

Figure 15. *Cont.*

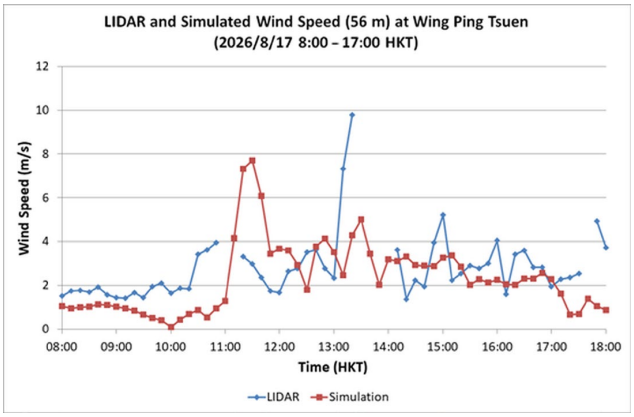

(**b**)

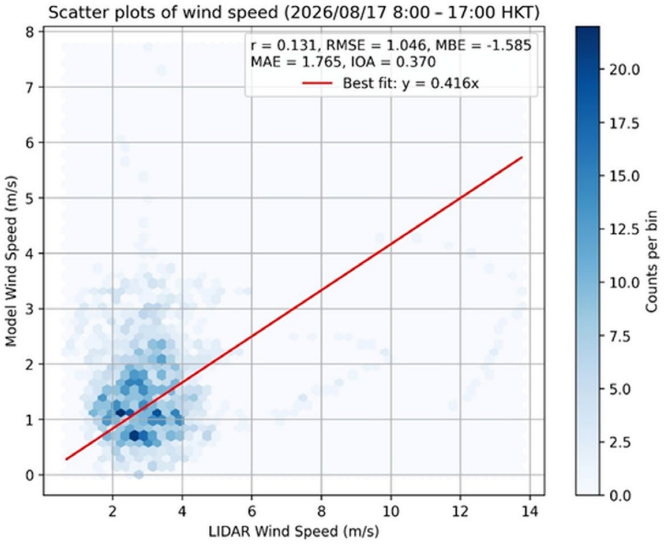

(**c**)

Figure 15. Time series of LIDAR observations and WRF simulation results at 56 m above ground level (**a**,**b**); (**c**) scatter plot of wind speeds at all heights.

Table 4 consolidates the statistical comparison for the three flights and the two Shenzhen Bay configurations. The bias is negative for wind speed and for the prognostic SGS TKE in all cases, indicating systematic underestimation.

Table 4. Summary statistics for the UAS–FastEddy comparisons. Bias is the mean model-minus-observation difference; MAE is the mean absolute error; RMSE is the root-mean-square error. Negative bias indicates model underestimation. The UAS statistics are indicative rather than formal validation (Section 2); r is not reported because a pointwise correlation along a moving trajectory conflates spatial and temporal variability.

Comparison	Bias	MAE	RMSE
	Wind speed (m s^{-1})		
Flight 1 (Long Ke Wan)	−1.86	2.60	3.26
Flight 2 (Science Park)	−2.67	2.92	3.57
Flight 3 (Shenzhen Bay, buildings)	−1.92	2.07	2.57
Flight 3 (Shenzhen Bay, no buildings)	−1.47	1.80	2.32
	TKE (m^2 s^{-2})		
Flight 1 (Long Ke Wan)	−1.31	1.31	1.65
Flight 2 (Science Park)	−0.92	0.96	1.41
Flight 3 (Shenzhen Bay, buildings)	−0.22	0.22	0.33
Flight 3 (Shenzhen Bay, no buildings)	−0.18	0.21	0.31

6. Limitations

The findings of this study should be interpreted in light of several limitations. First, only three flight cases are considered; while they span different locations, seasons and UAS platforms, they are insufficient to establish general model performance, and the conclusions drawn are case-specific hypotheses pending validation with a larger sample. Second, the 1 Hz UAS data resolve turbulent scales that are partly subgrid in the 20 m FastEddy mesh, and the UAS-derived TKE estimate uses only two components (w' is assumed zero), which biases the estimate low, while platform attitude can bias it high; the net observational bias is unknown. The TKE magnitude discrepancy is therefore partly an artifact of the model–observation scale mismatch and of the observational definition rather than a pure model error. Third, because WRF itself is biased (notably at Shenzhen Bay, $r = 0.13$ against LIDAR), the FastEddy error cannot be fully separated from the mesoscale driver error with the present experiment design. Fourth, the Keeta FP400-V4 wind estimates rely on a proprietary flight-control algorithm whose independent validation was not possible within this study; the associated observational uncertainty contributes to the model–observation gap. Fifth, no sensitivity analysis on grid resolution, timestep, spin-up period or turbulence parameters has been performed, owing to the substantial GPU computational cost of FastEddy at 20 m resolution; the chosen configuration follows the FastEddy best-practice recommendations and prior LES studies, but its optimality for low-building environments remains to be established. These limitations are reflected in the moderated conclusions below and define the priorities for follow-on work. Accordingly, the observed wind-speed and TKE under-estimation is attributed, as testable hypotheses for follow-on experiments, to (i) model–observation scale mismatch (1 Hz UAS vs. 20 m FastEddy grid), (ii) biased WRF boundary/initial forcing, (iii) excessive resolved-building drag and/or overestimated surface roughness for low-lying structures, and (iv) UAS-derived observational uncertainty (including the proprietary wind estimation of flight 2). These remain hypotheses rather than demonstrated causes; the present experiments cannot apportion the error among them.

7. Conclusions

The meteorological data collected by UAS along three routes in three separate locations during different seasons in Hong Kong were used to evaluate the FastEddy model for its potential application to provide meteorological support for drone operations in LAE. Two different UASs were used to ensure diversity in measurement platforms. For one case (flight no. 2), two different models were used, namely, the FastEddy model through mesoscale meteorological model-CFD model coupling, and the WRF model with BEP (in the so-called Urban Model) without explicit representation of the buildings. Apart from data collected from UAS, LIDAR data have been used in the evaluation where available. Although the number of cases is limited, the diversity in measurement platforms, assessment data types and simulation approaches provides useful insight into meteorological support for UAS operations. Across the three cases examined, the two simulation approaches tend to underestimate the measured wind speed. The FastEddy prognostic SGS TKE is lower than the UAS-derived TKE estimate in all three cases. Because the UAS estimate uses only two components (w' is assumed zero) and can be affected by platform attitude, while the model value is a subgrid quantity, this difference is interpreted as an indicative magnitude discrepancy rather than a direct model bias; its causes remain hypotheses. The simulated TKE fields are nonetheless qualitatively consistent in spatial pattern with the UAS-derived estimates and provide further insight into the complexity of turbulence distribution in the areas of UAS operations, even though these are not densely populated urban areas. The treatment of turbulent flow around relatively low buildings requires further study in FastEddy, as illustrated by the example flight in this paper.

Rather than providing an "ultimate solution" for wind and TKE simulation in support of UAS operations, this paper highlights several limitations of the current simulation approaches. Further refinement of the meteorological models is still required, and additional assessments should be conducted under different meteorological conditions and building/terrain configurations. Moreover, this paper calls for more urgent attention to TKE measurement on UAS platforms, including emerging LIDAR-based turbulence-retrieval techniques [28]. Additional TKE measurements, e.g., by LIDAR or by dedicated sonic-anemometer UAS platforms [14], may be required, in order to provide a more realistic assessment of the quality of simulated TKE by the various approaches. Further studies on these aspects will be reported in the future. The conclusions above therefore apply to the three cases reported here and should be regarded as hypotheses for broader validation; the computational cost of FastEddy at 20 m resolution (order of hours of GPU time per simulated hour) currently precludes an exhaustive sensitivity study, which is planned as follow-on work.

Author Contributions: Conceptualization, P.W.C.; Methodology, M.C.L., Y.F.L., K.K.L., S.N.C., P.W.C.; Software, K.K.L. and Y.K.; Validation, M.C.L., Y.F.L., Y.K.; Formal analysis, K.K.L., Y.K., E.D.; Investigation, K.K.L., S.N.C., Y.K.; Resources, P.W.C.; Data curation, M.C.L., Y.F.L.; Writing—original draft, P.W.C., Y.F.L.; Supervision, P.W.C.; Project administration, P.W.C. All authors have read and agreed to the published version of the manuscript.

Funding: This research received no external funding.

Institutional Review Board Statement: Not applicable.

Informed Consent Statement: Not applicable.

Data Availability Statement: The raw data supporting the conclusions of this article will be made available by the authors on request.

Acknowledgments: The authors gratefully acknowledge Keeta Drone for providing access to the wind information estimated from drone flight data used in this study. We thank Keeta Drone for its assistance with data preparation and sharing.

Conflicts of Interest: The authors declare no conflicts of interest.

References

1. Aldao, E.; Fontenla Carrera, G.; Veiga-López, F.; González-Jorge, H.; Martín, E. Turbulence-aware UAV path planning in urban environments. In Proceedings of the 2024 International Conference on Unmanned Aircraft Systems (ICUAS), Chania, Greece, 4–7 June 2024; pp. 280–285. [CrossRef]
2. Maronga, B.; Banzhaf, S.; Burmeister, C.; Esch, T.; Forkel, R.; Fröhlich, D.; Fuka, V.; Gehrke, K.F.; Geletič, J.; Giersch, S.; et al. The Parallelized Large-Eddy Simulation Model (PALM) version 4.0 for atmospheric and oceanic flows: Model formulation, recent developments, and future perspectives. *Geosci. Model Dev.* **2015**, *8*, 2515–2551. [CrossRef]
3. Giersch, S.; El Guernaoui, O.; Raasch, S.; Sauer, M.; Palomar, M. Atmospheric flow simulation strategies to assess turbulent wind conditions for safe drone operations in urban environments. *J. Wind Eng. Ind. Aerodyn.* **2022**, *229*, 105136. [CrossRef]
4. Elmeligy, M.M.; El-Rabbany, A.; Abdelrahman, S.M.; Mohasseb, M.; Hassaan, M.A.; Majidiyan, H. UAS-validated comparison of Sentinel-2 shoreline extraction techniques for large-lake coastal mapping. *Technologies* **2026**, *14*, 459. [CrossRef]
5. Hon, K.K.; Chan, P.W.; Chiu, Y.Y.; Tang, W.K. Application of short-range LIDAR in early alerting for low-level windshear and turbulence at Hong Kong International Airport. *Adv. Meteorol.* **2014**, *2014*, 162748. [CrossRef]
6. Chan, P.W.; Hon, K.K.; Shin, D.K. Combined use of headwind ramps and gradients based on LIDAR data in the alerting of low-level windshear and turbulence. *Meteorol. Z.* **2011**, *20*, 661–670. [CrossRef] [PubMed]
7. Lam, M.C.; Leung, W.H.; Lo, K.W.; Lai, K.K.; Chan, P.W.; He, J.Y.; Li, Q.S. A pilot study on meteorological support for the low-altitude economy—Consistency of meteorological measurements on UAS with numerical simulation results. *Atmosphere* **2026**, *17*, 107. [CrossRef]
8. Leung, W.H.; Lam, M.C.; Lai, K.K.; Chan, P.W. Evaluation and comparison of meteorological measurements by a UAS with high-resolution numerical weather prediction simulations. *Appl. Sci.* **2026**, *16*, 5521. [CrossRef]

9. Sauer, J.A.; Muñoz-Esparza, D. The FastEddy® resident-GPU accelerated large-eddy simulation framework: Model formulation, dynamical-core validation and performance benchmarks. *J. Adv. Model. Earth Syst.* **2020**, *12*, e2020MS002100. [CrossRef]
10. Muñoz-Esparza, D.; Shin, H.H.; Sauer, J.A.; Steiner, M.; Hawbecker, P.; Boehnert, J.; Pinto, J.O.; Kosović, B.; Sharman, R.D. Efficient graphics processing unit modeling of street-scale weather effects in support of aerial operations in the urban environment. *AGU Adv.* **2021**, *2*, e2021AV000432. [CrossRef]
11. Welch, B.M.; Horel, J.D.; Sauer, J.A. Application of the NCAR FastEddy® microscale model to a lake breeze front. *Atmosphere* **2024**, *15*, 809. [CrossRef]
12. Chen, D.; Su, W.; Jiang, S.; Yang, H.; Zhang, C.; Jiang, S.; Chang, D.; Liang, Y.; Wang, H.; Yang, X.; et al. Wind estimation based on flight dynamics of unmanned aerial vehicle: Influencing variables and its environmental application. *Atmos. Chem. Phys.* **2026**, *26*, 3607–3620. [CrossRef]
13. Compere, M.D.; Adkins, K.A.; Muthu Krishnan, A. Go with the flow: Estimating wind using uncrewed aircraft. *Drones* **2023**, *7*, 564. [CrossRef]
14. Ghirardelli, M.; Tampieri, F.; Schiaparelli, G.; Busetto, G. SAMURAI-S: Sonic anemometer on a multi-rotor drone for atmospheric turbulence investigation in a sling load configuration. *Atmos. Meas. Tech.* **2025**, *18*, 2103–2124. [CrossRef]
15. Skamarock, W.C.; Klemp, J.B.; Dudhia, J.; Gill, D.O.; Liu, Z.; Berner, J.; Wang, W.; Powers, J.G.; Duda, M.G.; Barker, D.M.; et al. *A Description of the Advanced Research WRF Model, Version 4.3*; NCAR Technical Note NCAR/TN-556+STR; National Center for Atmospheric Research: Boulder, CO, USA, 2019; p. 145. [CrossRef]
16. Iacono, M.J.; Delamere, J.S.; Mlawer, E.J.; Shephard, M.W.; Clough, S.A.; Collins, W.D. Radiative forcing by long-lived greenhouse gases: Calculations with the AER radiative transfer models. *J. Geophys. Res. Atmos.* **2008**, *113*, D13103. [CrossRef]
17. Niu, G.-Y.; Yang, Z.-L.; Mitchell, K.E.; Chen, F.; Ek, M.B.; Barlage, M.; Kumar, A.; Manning, K.; Niyogi, D.; Rosero, E.; et al. The community Noah land surface model with multiparameterization options (Noah-MP): 2. Evaluation over global river basins. *J. Geophys. Res. Atmos.* **2011**, *116*, D12110. [CrossRef]
18. Hong, S.-Y.; Noh, Y.; Dudhia, J. A new vertical diffusion package with an explicit treatment of entrainment processes. *Mon. Weather Rev.* **2006**, *134*, 2318–2341. [CrossRef]
19. Thompson, G.; Field, P.R.; Rasmussen, R.M.; Hall, W.D. Explicit forecasts of winter precipitation using an improved bulk microphysics scheme. Part II: Implementation of a new snow parameterization. *Mon. Weather Rev.* **2008**, *136*, 5095–5115. [CrossRef]
20. Lilly, D.K. *On the Application of the Eddy Viscosity Concept in the Inertial Sub-Range of Turbulence*; NCAR Manuscript No. 123; National Center for Atmospheric Research: Boulder, CO, USA, 1966; p. 19. [CrossRef]
21. Lilly, D.K. The representation of small-scale turbulence in numerical simulation experiments. In Proceedings of the IBM Scientific Computing Symposium on Environmental Sciences, New York, NY, USA, 14–16 November 1967; pp. 195–210.
22. Smagorinsky, J. General circulation experiments with the primitive equations: I. The basic experiment. *Mon. Weather Rev.* **1963**, *91*, 99–164. [CrossRef]
23. Zanaga, D.; Van De Kerchove, R.; Daems, D.; De Keersmaecker, W.; Brockmann, C.; Kirches, G.; Wevers, J.; Cartus, O.; Santoro, M.; Fritz, S.; et al. *ESA WorldCover 10 m 2021 v200*; Zenodo: Geneva, Switzerland, 2022. [CrossRef]
24. Stull, R.B. *An Introduction to Boundary Layer Meteorology*; Kluwer Academic Publishers: Dordrecht, The Netherlands, 1988; p. 666.
25. Martilli, A.; Clappier, A.; Rotach, M.W. An urban surface exchange parameterisation for mesoscale models. *Bound.-Layer Meteorol.* **2002**, *104*, 261–304. [CrossRef]
26. Salamanca, F.; Krpo, A.; Martilli, A.; Clappier, A. A new building energy model coupled with an urban canopy parameterization for urban climate simulations—Part I. Formulation, verification, and sensitivity analysis of the model. *Theor. Appl. Climatol.* **2010**, *99*, 331–344. [CrossRef]
27. Lai, S.K.; Chan, P.W.; He, Y.; Chen, S.S.; Kerns, B.W.; Su, H.; Mo, H. Real-time operational trial of atmosphere–ocean–wave coupled model for selected tropical cyclones in 2024. *Atmosphere* **2024**, *15*, 1509. [CrossRef]
28. Luce, H.; Yabuki, M. Turbulence kinetic energy dissipation rate estimated from a WindCube Doppler lidar and the LQ7 1.3 GHz radar wind profiler in the convective boundary layer. *Atmos. Meas. Tech.* **2025**, *18*, 1193–1208. [CrossRef]

Disclaimer/Publisher's Note: The statements, opinions and data contained in all publications are solely those of the individual author(s) and contributor(s) and not of MDPI and/or the editor(s). MDPI and/or the editor(s) disclaim responsibility for any injury to people or property resulting from any ideas, methods, instructions or products referred to in the content.